A&A 596, A79 (2016)
DOI: 10.1051/0004-6361/201628555

Astronomy & Astrophysics

Timing the warm absorber in NGC 4051

C. V. Silva[1,2], P. Uttley[1], and E. Costantini[2]

[1] Anton Pannekoek Institute for Astronomy, University of Amsterdam, Science Park 904, 1098 XH Amsterdam, The Netherlands
e-mail: c.v.dejesussilva@uva.nl
[2] SRON, Netherlands Institute for Space Research, Sorbonnelaan 2, 3584 CA Utrecht, The Netherlands

Received 18 March 2016 / Accepted 3 July 2016

ABSTRACT

We investigated, using spectral-timing analysis, the characterization of highly ionized outflows in Seyfert galaxies, the so-called warm absorbers. Here, we present our results of the extensive ~600 ks of *XMM-Newton* archival observations of the bright and highly variable Seyfert 1 galaxy NGC 4051 whose spectrum has revealed a complex multicomponent wind. Making use of both RGS and EPIC-pn data, we performed a detailed analysis through a time-dependent photoionization code in combination with spectral and Fourier spectral-timing techniques. The source light curves and the warm absorber parameters obtained from the data were used to simulate the response of the gas to variations in the ionizing flux of the central source. The resulting time variable spectra were employed to predict the effects of the warm absorber on the time lags and coherence of the energy dependent light curves. We have found that, in the absence of any other lag mechanisms, a warm absorber with the characteristics of the one observed in NGC 4051, is able to produce soft lags, up to 100 s, on timescales of hours. The time delay is associated with the response of the gas to changes in the ionizing source, either by photoionization or radiative recombination, which is dependent on its density. The range of radial distances that, under our assumptions, yield longer time delays are distances $r \sim 0.3{-}1.0 \times 10^{16}$ cm, and hence gas densities $n \sim 0.4{-}3.0 \times 10^{7}$ cm^{-3}. Since these ranges are comparable to the existing estimates of the location of the warm absorber in NGC 4051, we suggest that it is likely that the observed X-ray time lags may carry a signature of the warm absorber response time to changes in the ionizing continuum. Our results show that the warm absorber in NGC 4051 does not introduce lags on the short timescales associated with reverberation, but will likely modify the hard continuum lags seen on longer timescales, which in this source have been measured to be on the order of ~50 s. Hence, these results highlight the importance of understanding the contribution of the warm absorber to the AGN X-ray time lags since it is also vital information for interpreting the lags associated with propagation and reverberation effects in the inner emitting regions.

Key words. methods: data analysis – black hole physics – galaxies: Seyfert – galaxies: individual: NGC 4051 – quasars: absorption lines – X-rays: galaxies

1. Introduction

Active galactic nuclei (AGN) are powered by accretion onto a supermassive black hole ($10^6{-}10^9$ $M_\odot$). Outflowing events are often also associated with AGN. This ejection of matter and energy, if powerful enough, may affect the surrounding environment of the AGN and even disturb the evolution of the host galaxy or the cluster hosting the AGN, a phenomenon often termed AGN feedback (e.g. Di Matteo et al. 2005; Hardcastle et al. 2007; Fabian 2012; Crenshaw & Kraemer 2012). The impact of the outflows on the surrounding environment is a function of their distance to the central source, the column density of the outflowing gas, and is highly dependent on the outflowing velocities. Hence, it is crucial to investigate the physical properties of the gas in order to assess its importance for feedback. However, while the column density and the outflowing velocity of the gas are inferred from observations, it is not possible to directly estimate the distance of the gas to the central source.

In the case of Seyfert 1 galaxies, 60% show the presence of highly ionized outflowing absorbing gas that is rich in metals (Crenshaw et al. 1999). The outflowing material, usually called a warm absorber, is remarkably complex in structure, spanning a wide range of ionization parameters, outflowing velocities, and column densities. These outflows have been detected both in the UV and in the X-ray spectra of Seyfert 1 galaxies through a composite set of absorption lines (for a review see Crenshaw et al. 2003). Determining the radial location of the outflows yields valuable information for the study of AGN feedback. However, characterizing the spatial location of the warm absorbers is not trivial. A common approach to determinining the distance of the absorber to the central source is measuring the density n of the gas using sensitive absorption lines, and deriving the distance r through the ionization parameter ξ, where $\xi = L_{\rm ion}/nr^2$ (e.g. Kraemer et al. 2006; Arav et al. 2008). This method is usually successful for UV data, where these lines are more commonly found, but it is not very effective in studying warm absorbers in the X-rays (e.g. Kaastra et al. 2004). There we lack the instrumental sensitivity necessary to achieve such measurements. Alternatively, monitoring the response of the gas to changes in the ionizing continuum leads to an estimation of a recombination timescale, which is a function of the electron density. This approach has been applied through time-resolved spectroscopy studies and time-dependent photoionization models (Behar et al. 2003; Reeves et al. 2004; Krongold et al. 2007; Steenbrugge et al. 2009; Kaastra et al. 2012). Time-resolved spectroscopy in the X-rays suffers from the problem that the involved timescales may be on the order of minutes to hours, which yields limited photon counts per time and energy bin; instead, the issue of low signal to noise can be avoided by studying the statistical properties of variability through the use of Fourier spectral-timing techniques.

Fourier spectral-timing techniques have been applied to the study of AGN X-ray light curves for more than a decade. It has been found in many sources that soft and hard X-ray photons behave differently on different timescales. For long timescales, the hard photons arrive with a time delay compared to the soft photons. On the contrary, on short timescales the soft photons lag behind the hard photons. The complex timescale-dependent lags are associated with different physical processes and disentangling them is essential to understanding the innermost emitting regions in AGN. The soft lag associated with short timescales has been explained through reverberation from reflected emission (Fabian et al. 2009). This scenario is supported by the recently found Fe Kα lags (Zoghbi et al. 2012; Kara et al. 2013). Furthermore, it has been suggested that fluctuations in the accretion flow propagate inwards so that the outermost soft X-rays respond faster than the innermost hard X-rays, which could explain the hard lag seen on long timescales (Kotov et al. 2001; Arévalo & Uttley 2006). Most of the AGN that show such timing properties, are Seyfert 1 galaxies. Since most Seyfert 1 galaxies show the presence of a warm absorber, our goal in this paper is to explore the possible contribution of the warm absorber to the observed X-ray time lags due to the delayed response of the gas to the continuum variations.

In this work we expand on the method of Kaastra et al. (2012), using a time-dependent photoionization model to examine the response of the gas to changes in the ionizing continuum. NGC 4051, a relatively nearby Seyfert 1 galaxy ($z \approx 0.002$), is an ideal candidate for this study. This source is not only bright (with a luminosity in the 2−10 keV band of $L_X \sim 2.1 \times 10^{41}$ erg s^{-1} and a corresponding observed flux of $f_X \sim 1.6 \times 10^{-11}$ erg s^{-1} cm^{-2} in the data used here), but also highly variable (McHardy et al. 2004) and has been associated with a complex multicomponent warm absorber (Steenbrugge et al. 2009; Pounds & Vaughan 2011). NGC 4051 also shows the characteristic X-ray time lags found in other AGN (Alston et al. 2013a): a hard lag at low frequencies and a soft lag at high frequencies. Furthermore, NGC 4051 has an extensive series of *XMM-Newton* archival observations. In Sect. 2 we present the methods used in the reduction and processing of the raw data products, and also the procedures used to extract the light curves and spectra. In Sect. 3 we simulate the response of the complex warm absorber observed in the energy spectra of NGC 4051 to changes in the luminosity of the central source, and the dependence of this response on radial distance and density. In Sect. 4 we further investigate whether a non-equilibrium gas phase, which results in a delayed response of the gas to the variations in the central source, could produce a time delay of the most absorbed X-ray bands relative to the broad X-ray ionizing continuum. Finally, we compare our simulations to the real data in Sect. 5 and present our conclusions in Sect. 6.

Throughout this work we use a flat cosmological model with $\Omega_m = 0.3$, $\Omega_\Lambda = 0.7$, and $\Omega_r = 0.0$, together with a cosmological constant $H_0 = 70$ km s^{-1} Mpc^{-1}. For the spectral modeling in this paper we have assumed a Galactic column density of $N_H = 1.15 \times 10^{20}$ cm^{-2} (Kalberla et al. 2005). The errors quoted in this paper are 1σ errors unless otherwise stated.

2. Observations and data reduction

NGC 4051 has been extensively observed by *XMM-Newton*. We make use of the 15 observations from 2009, a total of ~570 ks of data (see Vaughan et al. 2011, for details).

2.1. RGS and EPIC-pn light curves

The observation data files (ODFs) were reprocessed using the *XMM-Newton* Science Analysis System (SAS v.13.5) to generate calibrated event lists for RGS and for EPIC-pn where the conditions `PATTERN<=4` and `FLAG=0` were used. For the purposes of this work, RGS and EPIC-pn event lists were filtered through a common good time intervals (GTI) file, created with the task MGTIME from HEASOFT (v. 6.15), to only include time intervals in which RGS and EPIC-pn were simultaneously observing. For EPIC-pn we extracted source and background event lists by selecting circular regions with a radius of 20 arcsec. All the observations were inspected for high particle background flaring and this was properly accounted for in the filtering process.

RGS background subtracted light curves were extracted with the SAS task RGSLCCORR, for the two RGS instruments combined and first order selected, with a time binsize of 100 s. EPIC-pn background subtracted light curves were obtained by using the RGS light curves as templates for start and stop times, and for binsize, such that both RGS and EPIC-pn light curves are evenly sampled in time. This was done for each observation separately (see Fig. 1). The light curves were also corrected for short exposure losses by linear interpolation of the nearest good data points in each side, adding appropriate Poisson noise (as seen in Vaughan et al. 2011).

2.2. RGS and EPIC-pn spectra

RGS spectra (source and background) together with response matrix files (RMFs) were extracted for each observation by using SAS, selecting first order. The averaged RGS spectrum was obtained using the SAS task RGSCOMBINE which combines the spectra of all observations and creates a single RMF. Source and background EPIC-pn spectra were extracted with SAS for each observation, simultaneously with the corresponding RMFs and ancillary response files (ARFs). Using HEASOFT (v.6.15), we produced a time-averaged EPIC-pn spectrum both for the source and for the background, adding the individual spectra with the ftool MATHPHA. To combine the response matrix and effective area files we made use of the ftools ADDRMF and ADDARF.

3. Time-dependent photoionization model

The main goal in this paper is to study the possible effects of a warm absorber on the spectral-timing data from NGC 4051. To this end, we perform a detailed study of the response of the outflowing gas to the fast changes in the ionizing continuum. Using a time-dependent photoionization model we investigate the variations in the spectrum due to a complex warm absorber illuminated by a variable continuum source. The correct modeling of the energy spectrum as a function of time will allow us to generate light curves which are dependent on the flux history of the source.

For photoionization, a variable X-ray source has an effect on the ionization balance of the gas. The outflowing gas, which is rich in metals, responds to the changes in the ionizing flux in the following manner. When the flux of the ionizing source increases, the gas becomes more ionized. In the same way, when the flux of the ionizing source decreases, the gas recombines. In order to monitor the time evolution of the ion concentrations in the gas, it is necessary to solve the time-dependent ionization balance equations. As such, the relative density n_{X^i} of ion i of a certain species X varies with time as a function of the electron density of the gas n_e, the recombination rate from stage $i+1$ to i

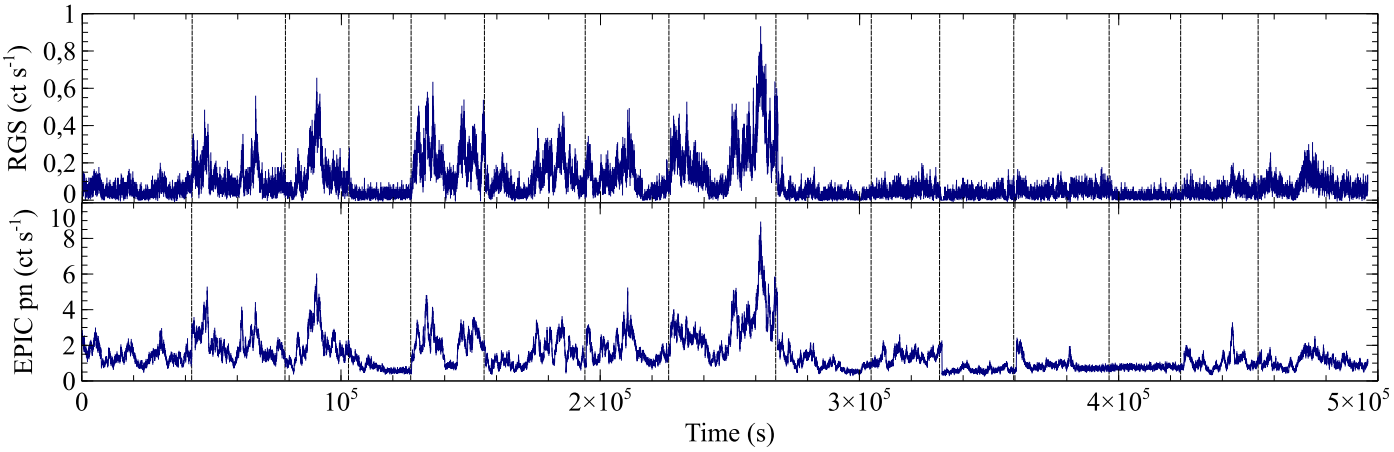

Fig. 1. RGS light curves for the 15−17 Å band (*top*) and EPIC-pn light curves for 1.5−10 keV (*bottom*). The dashed lines separate each individual observation.

(given by the recombination coefficient $\alpha_{\mathrm{rec}\,\mathrm{X}^i}$ times the electron density), and the ionization rate from stage i to $i+1$, I_{X^i}. This time dependence is given by Krolik & Kriss (1995), and can be written as

$$\frac{\mathrm{d}n_{\mathrm{X}^i}}{\mathrm{d}t} = -n_{\mathrm{X}^i} n_{\mathrm{e}} \alpha_{\mathrm{rec,X}^{i-1}} - n_{\mathrm{X}^i} I_{\mathrm{X}^i} + n_{\mathrm{X}^{i+1}} n_{\mathrm{e}} \alpha_{\mathrm{rec,X}^i} + n_{\mathrm{X}^{i-1}} I_{\mathrm{X}^{i-1}} \quad (1)$$

in which Auger ionization, collisional ionization, and three-body recombination were neglected. Equation (1) is thus defined by the sum of the destruction rate and formation rate of each ion only due to photoionization and radiative recombination.

If this response is instantaneous, the gas is in photoionization equilibrium with the ionizing continuum at all times. However, this has been shown to not always be the case and so the processes of ionization and recombination of the gas can be associated with ionization and recombination timescales. Ionization and recombination timescales correspond to the time it takes for the gas to reach equilibrium with the ionizing continuum for increasing or decreasing flux phases, respectively. Following Nicastro et al. (1999)[1], this timescale can be approximated as

$$t_{\mathrm{eq}}^{\mathrm{X}^i,\mathrm{X}^{i+1}} \sim \left(\frac{1}{\alpha_{\mathrm{rec,X}^i} n_{\mathrm{e}}}\right) \times \left[\frac{1}{-(\alpha_{\mathrm{rec,X}^{i-1}}/\alpha_{\mathrm{rec,X}^i}) + (n_{\mathrm{X}^{i+1}}/n_{\mathrm{X}^i})}\right]. \quad (2)$$

In this situation, the gas will reach equilibrium with the ionizing continuum after a time delay t_{eq}. Since the equilibrium timescale shows a dependence on the electron density, measuring this time delay would allow us to constrain the density of the gas. The same time delay could also produce an overall delay effect of the more absorbed energy bands relative to the continuum, which could affect the X-ray lag measurements in these systems. We investigate this possibility in detail in Sect. 4.

Another possibility for the behavior of this gas is that its response time is much longer than the typical variability timescales of the source. In this case the gas is in a steady state, but never reaches equilibrium with the ionizing continuum (Krolik & Kriss 1995). At best, the densities of the ions remain fairly constant around their mean values: the ionization and recombination rates correspond to the values associated with the mean flux of the source over time.

All this complex behavior can be assessed by solving Eq. (1) and studying the time dependence of the ions. Our approach to obtaining the time-dependent ion concentrations follows that of Kaastra et al. (2012). The whole method is described below, including some results from the simulations we performed with the calculated concentrations.

[1] The analytical approximation for the response time, given here by Eq. (2), has been corrected for a typo in the expression from Nicastro et al. (1999) where the minus sign in the denominator is missing.

3.1. Ionizing continuum

NGC 4051 is highly variable, showing large variations in flux over relatively short timescales, on the order of few hours (McHardy et al. 2004; Vaughan et al. 2011). This intrinsic rapid variability, together with its complex absorbed spectrum, makes NGC 4051 an ideal candidate for this study. The ionizing continuum used to obtain the ionization balance takes as reference the time-averaged spectral energy distribution (SED) of the 15 observations of NGC 4051 mentioned in Sect. 2. It is important to note here that for the purpose of our study we assume that the ionizing continuum only changes in X-ray flux normalization. The shape of the SED that we consider here is kept constant with time. The reason is to not include any other source of lags due to the continuum variations. In this way, the light curves we generate are only affected by the variable warm absorber (excluding any effects due to changes in the spectral shape, with time, which naturally introduces time delays between different energy bands). For details see Sect. 3.5.

The X-ray shape of the SED is taken from the time-averaged spectrum of EPIC-pn. We have performed a phenomenological fit using the spectral fitting package SPEX v.2.05 (Kaastra et al. 1996) to obtain the time-average shape of the broad X-ray spectrum (0.5−10 keV). The model used to describe the overall shape of the continuum consists of a steep power law ($\Gamma \sim 3.02$) with a spectral break at ∼1.47 keV, which leads to a harder spectrum ($\Gamma \sim 1.75$). To better model the spectrum in the soft band, where strong absorption features are detected in the RGS data, we add a set of warm absorption models. These absorption models result from fitting the time-averaged RGS spectrum using the XABS model from SPEX, corresponding to absorption by a slab of material in photoionization equilibrium. In this step we use the default ionization balance in SPEX, set by running CLOUDY v.13.01 (Ferland et al. 2013) with a standard SED shape from NGC 5548. This is a good approximation since at this stage we only aim to constrain the overall shape of the EPIC-pn spectrum, and the changes that the appropriate ionization balance introduces are small at the available resolution. Furthermore, a positive Gaussian profile centered at ∼6.44 keV, with width

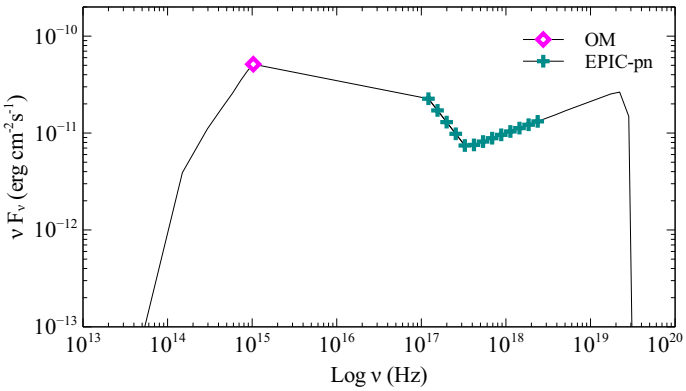

Fig. 2. Spectral energy distribution of NGC 4051 for the averaged EPIC-pn and OM data.

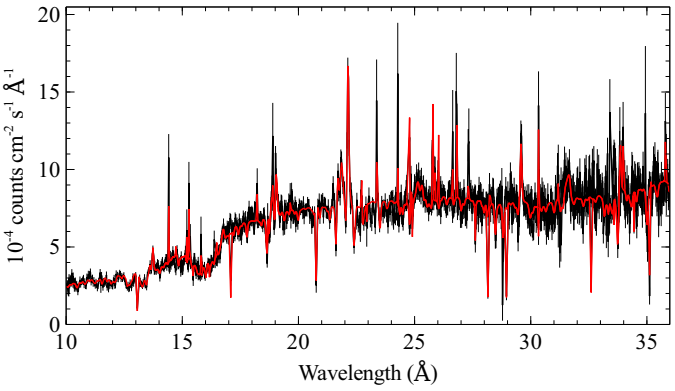

Fig. 3. Best fit model (in red) of the time-averaged RGS spectrum (in black) of NGC 4051.

Table 1. Best fit parameters of the RGS spectrum for the multicomponent photoionized outflow.

Comp	$\log \xi$	$N_{\rm H}$ (10^{21} cm^{-2})	Flow velocity (km s^{-1})
1	2.99 ± 0.03	3.3 ± 0.4	-4260 ± 60
2	3.70 ± 0.04	16.1 ± 0.5	-5770 ± 30
3	2.60 ± 0.10	1.2 ± 0.2	-530 ± 10
4	0.37 ± 0.03	0.11 ± 0.09	-340 ± 10

$\sigma \sim 160$ eV, was added to account for the Fe K feature visible in the spectrum.

To complete the time-averaged SED we made use of the OM data, which are also available for these observations. The OM data were collected in Imaging mode in the UVW1 filter, corresponding to a central wavelength of 2910 Å (see Alston et al. 2013b, for more details). The OM count rates were extracted with SAS task OMCHAIN and converted to fluxes by using the recommended conversion factor. We took the average flux of the 15 observations and used this value as the time-averaged flux at 2910 Å. Beyond the OM data, we made use of the default AGN continuum in CLOUDY, which is characterized by relatively low luminosity at longer wavelengths (Mathews & Ferland 1987). The SED was completed by expanding the continuum above 10 keV, adding an artificial cutoff at ~150 keV. The broadband SED is presented in Fig. 2.

3.2. Multicomponent outflowing gas

To accurately model the time evolution of the ion concentrations in the gas, it is first necessary to model the RGS spectrum, taking into account the numerous absorption features observable in the 10−36 Å range. Considering that the continuum spectral shape is represented here in such a narrow energy band, we chose a phenomenological continuum model, which can better describe only the soft band. Therefore, we fit the underlying continuum of the time-averaged RGS spectrum with a blackbody emission component ($T \sim 0.15$ keV) in addition to a power-law model. The power law has an index $\Gamma \sim 3.1$. To account for the complex absorption features observed, we use the SPEX photoionization absorption model XABS. The ionization balance is calculated with CLOUDY, using the previously constructed SED (see Fig. 2). Our best fit results in the detection of four distinct photoionized components, summarized in Table 1.

To complete the fit, we also added radiative recombination continuum models where necessary and Gaussian profiles to account for visible emission lines. These narrow emission lines do not vary in flux, and so they will not contribute to any possible delay caused by the response time of the warm absorber. The best fit model is shown in Fig. 3. The four distinct outflowing components were first identified by Pounds & Vaughan (2011); however, the parameters of each component vary slightly when compared to our results. This discrepancy is likely due to two factors. First, we fit the time-averaged spectrum while Pounds & Vaughan (2011) have modeled the high-flux spectrum. Second, Pounds & Vaughan (2011) have calculated the physical conditions of the photoionized gas with XSTAR.

3.3. Ionization and recombination rates

To solve the time-dependent concentrations it is necessary to know the ionization and recombination rates, and the initial ion concentrations, at each point in the light curve. Starting at the beginning of the first observation, for which we assume photoionization equilibrium, we monitor the flux level every 500 s until the end of the last observation. We decided to track the flux history with this time resolution because the typical large amplitude variability occurs on timescales of hours, and because we would like to have a span of variability timescales that would allow us to make a comparison with previous results on X-ray time lags, typically reaching timescales of hundreds of seconds.

The equilibrium ion concentrations for each of the selected points in the light curve were calculated with CLOUDY using the source SED and Lodders et al. (2009) abundances. This is calculated for each gas component separately by feeding CLOUDY with the ionization parameter for each component, assuming equilibrium. This ionization parameter was obtained from fitting the time-averaged RGS spectrum, and it was then linearly scaled to account for the difference between the flux at each time bin and the average flux value. If the gas responds immediately to the variability of the ionizing continuum, then the gas ionization must change according to

$$\xi = \frac{L_{\rm ion}}{nr^2}, \tag{3}$$

where ξ is the ionization parameter and $L_{\rm ion}$ is the ionizing luminosity. The assumption here is that the distance of the gas from the ionizing source r and its density n remain constant for these timescales. Therefore, the average ξ values were just linearly scaled up or down according to the flux values at each time.

The ionization and recombination rates provided by CLOUDY were stored at the end of each run. The ionization rates obtained with CLOUDY include multiple ionization after inner-shell ionization. Since in Eq. (1) multiple ionization is not taken into account, we correct the ionization rates obtained to force equilibrium when inserting these in the equation together with the equilibrium concentrations, which needs to yield $dn_{X^i}/dt = 0$.

3.4. Time-dependent ion concentrations

Having all the prior information we need, we can now proceed to solve the time-dependent ion concentrations. Equation (1) corresponds to a system of N coupled ordinary differential equations. We first attempted to solve the system of differential equations numerically by using a Runge-Kutta method with adaptive step-size control, subroutine ODEINT (Press et al. 1992). However, our solution appeared to be *stiff*, i.e., the required step size was unacceptably small compared to the smoothness of the solution for a certain time interval. To account for the stiffness of the system we implemented in ODEINT a fourth-order Rousenbrock method, the subroutine STIFF (Press et al. 1992), which is a generalization of the Runge-Kutta method for stiff systems.

We performed the calculations for each outflow component separately, keeping the electron density n_e constant with time, as featured in Kaastra et al. (2012) and Nicastro et al. (1999). As for the initial conditions, we take the first point of the first observation to be $t_0 = 0$ and feed it with the equilibrium concentrations calculated with CLOUDY. Thus, we assume equilibrium at the start of the first observation. Thereafter, for each time step the ionization and recombination rates are obtained by linearly interpolating on the ionization and recombination rates we previously calculated with CLOUDY. These solutions are computed for a grid of distances r from the ionizing source. This allows us to explore the parameter space since the real location and density of the gas are unknown. From the observed spectrum it is possible to estimate the ionizing luminosity L_{ion} and the ionization parameter ξ for each outflowing component. From Eq. (3), it follows that – for a fixed moment in time – the product of the density of the gas with its squared distance to the source nr^2 is constant. Thus we assume that all the outflowing components are at a fixed distance from the central source, with a corresponding density n prescribed by the ratio L_{ion}/ξ. We then vary the distance r and calculate the time-dependent ion concentrations for the corresponding density of each component. An example of our results is shown in Fig. 4. The two upper panels in Fig. 4 display the time evolution of the relative concentration of Fe XI and Fe XIX, respectively, for component 1 in Table 1. The stars represent the equilibrium concentrations, e.g., the concentrations the gas would have if it responded instantaneously to the ionizing source variability. The colored solid lines refer to the calculated concentrations for different distances r from the ionizing source. As a reference, for component 1, $r \sim 10^{16}$ cm corresponds to a density $n \sim 3.6 \times 10^6$ cm^{-3}. Finally, the lower panel in the plot shows the light curve (0.3–10 keV), which is used to determine the variable ionizing flux for the same time interval.

It is interesting to note the different response of Fe XI and Fe XIX to changes in the ionizing flux. The outflowing component shown here has log $\xi \sim 2.99$. At the beginning, the flux is not very high and the relative concentration of Fe XI is large, while the relative concentration of Fe XIX is negligible. When the flux increases significantly, the less ionized Fe XI gets partially stripped in favor of its more ionized relative Fe XIX. This is exactly the behavior we expect, since a significant increase in flux will photoionize Fe and take it to its higher levels of ionization. Likewise, a significant decrease in flux will lead Fe to recombine and we will see a higher concentration of the less ionized levels. We use Fe as an example since it is sensitive to ionization parameters such as this one. Also worth noting in Fig. 4 is the detection of the three different kinds of possible behavior for the response of the gas relative to the ionizing continuum (see introduction to Sect. 3). For close distances to the ionizing source, the response is almost instantaneous. This is the case for distances $\leq 10^{14}$ cm where the response is immediate but the ion concentration may not have time to reach the equilibrium values before being disturbed again. For distances between $\sim 10^{15}$ cm and $\sim 10^{16.5}$ cm, the gas responds to the variations of the ionizing continuum with a visible time delay. This is the most interesting case for our study since it is the case for which a time lag associated with the response time of the gas relative to the continuum variability may be detected. Finally, at distances $\geq 10^{16.5}$ cm, the gas is unable to respond to the changes of the continuum flux. For distances so far from the central source, the gas is in a steady state and the relative ion concentrations vary slightly around a mean value corresponding to the mean flux level over time. We explore in Sect. 4 the effects that the complex behavior of the warm absorber can have on the X-ray time lags.

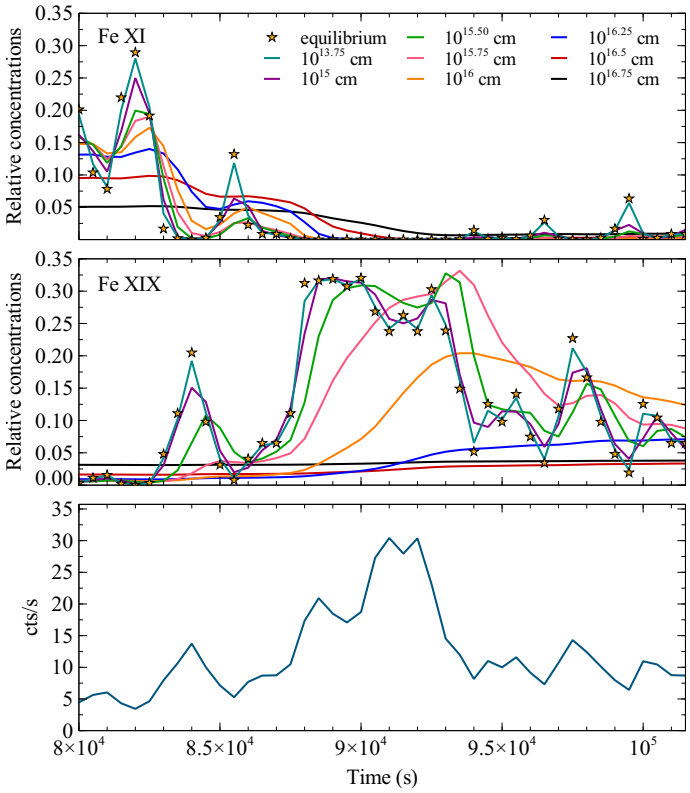

Fig. 4. Time-dependent evolution of the relative concentrations of Fe XI (*upper panel*) and Fe XIX (*middle panel*) responding to changes in the ionizing continuum (*lower panel*) for different distances of gas component 1 (see Table 1) from the ionizing source.

3.5. Simulated spectrum and light curve generation

In order to study the pure effects of a variable warm absorber on the X-ray time lags of NGC 4051, it is necessary to generate light curves that are only affected by the changes of the relative ion concentrations over time. We then proceeded to the simulation of RGS and EPIC-pn spectra, which we use later to build the necessary light curves for our analysis. The aim is to

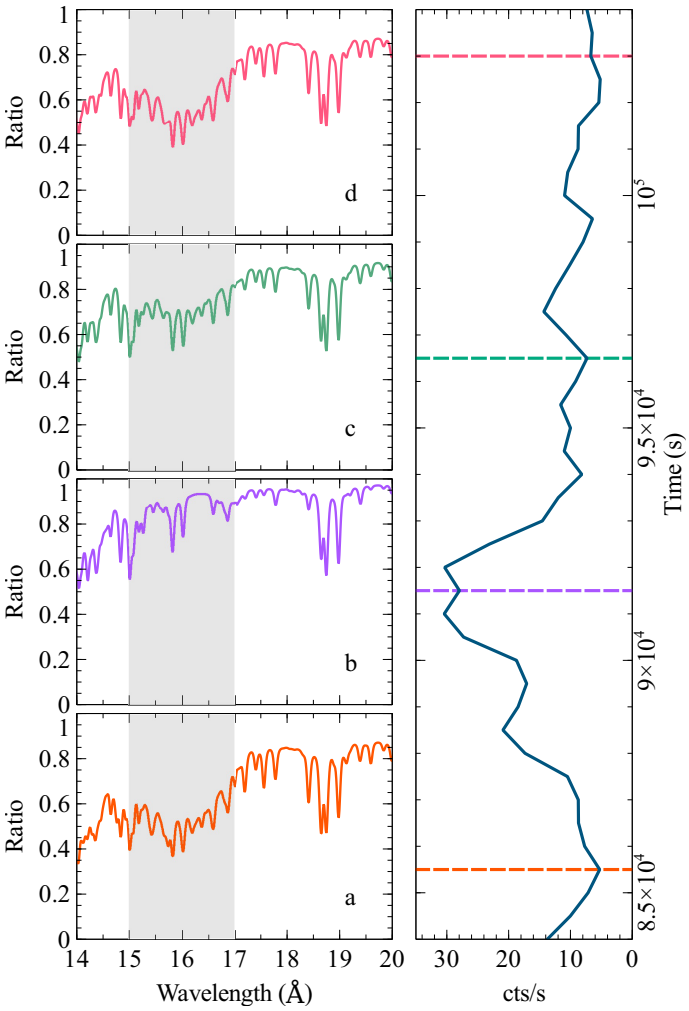

Fig. 5. *Left panel*: data/continuum model ratio of the simulated RGS spectra for $r = 10^{15.75}$ cm around the region of the Fe UTA complex (15−17 Å, gray area in the spectra) for distinct time steps indicated by the dashed lines on the right. *Right panel*: slice of the generated light curves from the simulated spectra, which includes the time steps of the spectra in the left. We note that spectra **a)**, **c)** and **d)** have approximately the same flux level but show different absorption features, which indicates the dependence of the warm absorber on the flux variation history.

construct new light curves with the same flux history as those of NGC 4051, but whose spectrum at each time step is only affected by the variable warm absorber.

Using SPEX, we simulate RGS and EPIC-pn spectra for each time step in the following manner. We included the predefined continuum shape (see Sects. 3.1 and 3.2) with the flux levels prescribed by the light curve. The shape of the spectrum is kept constant with time to avoid time delays caused by intrinsic changes in the X-ray continuum shape. To account for the variability in the ionizing source, we scale the flux level of the X-ray spectrum according to the count rate history of the X-ray light curves of NGC 4051. In fact, the spectral shape of NGC 4051 is highly variable with time. However, this should not invalidate our results because first, the absorption effects are stronger in the soft X-rays whereas the spectral-variability more strongly affects the shape of the continuum above ∼1 keV (see e.g. Uttley et al. 1999; Vaughan et al. 2011), and second, since the source count rate is dominated by the soft photons, the soft X-rays are a good proxy for the ionizing flux changes. This continuum is absorbed by a multilayer warm absorber; the ionic ion column densities are given by the time-dependent ion concentrations. This is achieved using the SLAB model from SPEX. The SLAB model is a thin slab absorption model, for which the ion column density can be chosen independently. The column densities are calculated for each ion with the time-dependent concentrations we computed previously. In this way each simulated spectrum is identical in underlying continuum shape, and is only changed by the variable column densities derived from the time-dependent concentrations. The complex warm absorber we find in the RGS data is also added to the EPIC-pn continuum since it must also be present there, only we do not have the spectral resolution to observe the narrow absorption features. The model is then folded through the instrumental response matrix to obtain the net count rate per energy channel. Since our purpose for now is to study the unadulterated effect of the variable warm absorber in the absence of observational noise, no Poisson noise was added to the simulations (for the implications of noise for lag detectability see Sect. 5.1). Examples of the simulated spectra are shown in Fig. 5 (left panel). The simulated spectra are subsequently used to generate light curves for all bands of interest, both for EPIC-pn and RGS. An example of the generated light curves is also shown in Fig. 5 (right panel). Furthermore, in Fig. 5 we observe the delayed response of the gas to the variations of the continuum. The figure shows the simulated spectra resulting from the calculated concentrations at $r = 10^{15.75}$ cm. As we can see from Fig. 4, the ion concentrations follow the light curve evolution with a significant time delay. This time delay is also detectable in a simple example in Fig. 5. From the time step represented in spectrum a to the time step represented in spectrum b, the flux increases by a factor of ∼3. The changes in the spectral features are visible. When the flux decreases to the same level as before – in the time step represented in spectrum c – the spectrum has not yet recovered the same features it had at the beginning. Some time later, at the time step represented in spectrum d, the spectrum finally starts to recover its initial shape for the same flux level. This is a signature of the time delay observed in Fig. 4 and, in this case, it is associated with a recombination timescale on the order of, at least, some hours.

These small changes in absorption are indeed responsible for any time delays, since no other variability processes are considered here. The absorption changes are small in general and will modulate only a small fraction of the total flux. These small modulations will introduce small variations in the distribution of flux in the light curves, which can then allow us to measure time delays between the absorbed bands and the continuum. In the next section we make use of the light curves generated with the simulated spectra and compute the spectral-timing products resulting from the application of Fourier methods.

4. Timing analysis

In the previous section we show how we generate light curves that contain only the flux variability plus the effects of the variations in the relative ion concentrations due to the intrinsic source variability, excluding the effects associated with variability of the continuum spectral shape. In this section, we analyze these time series in the Fourier domain and assess the effects of the variable warm absorber on the lag-frequency and lag-energy spectra of NGC 4051. In the next paragraphs we introduce the Fourier techniques commonly used to detect time lags in X-ray light curves. This is intended to give an introduction to timing analysis for readers who are not familiar with the subject. For more details about spectral-timing analysis on X-ray light curves of black hole systems of all scales see Uttley et al. (2014).

The most common tool in Fourier analysis is the Fourier power spectrum, or power spectral density function (PSD). The power spectrum contains information about the underlying structure of a stochastic variability process. It shows the dependence of the variability amplitude as a function of temporal frequency. However, we cannot simply measure the power spectrum. Since every observation is a random realization of the underlying PSD, what we actually measure is a noisy random realization, referred to as the periodogram. The periodogram is obtained from the discrete Fourier transform of the signal we are analyzing. Thus, we begin by introducing the discrete Fourier transform X_n of a time series x,

$$X_n = \sum_{k=0}^{N-1} x_k \exp(2\pi i n k/N), \tag{4}$$

where N is the number of time bins of width Δt and x_k is the value of the light curve at index k. The Fourier transform is evaluated at each Fourier frequency $f_n = n/(N\Delta t)$, with $n = 1, 2, ..., N/2$. Thus, the lowest Fourier frequency is $1/N\Delta t$, which corresponds to the inverse of the total observation time, and the highest Fourier frequency is $1/2\Delta t$, also known as the Nyquist frequency. The periodogram is defined as the modulus square of the Fourier transform of the time series x, $|X_n|^2$, which can be written as

$$|X_n|^2 = X_n^* X_n \tag{5}$$

where the X_n^* represent the complex conjugate of X_n. The periodogram can be normalized to yield the same units as the PSD and is usually computed for several light curve segments. It is subsequently binned over the segments, and also over frequency bins, to obtain an estimate of the underlying PSD, which can then be modeled. Following the notation in Uttley et al. (2014), we denote the binned periodogram $\overline{P}_X$.

We now consider two light curves, x and y, with x being a band of interest (typically a small energy bin) and y a broad reference band that excludes x. It is possible to derive the frequency-dependent lag between these two bands by applying the cross-spectrum method. The cross-spectrum is defined as

$$C_{XY,n} = X_n^* Y_n \tag{6}$$

and when considering the complex polar representation of the Fourier transforms, Eq. (6) takes the form

$$C_{XY,n} = A_{X,n} A_{Y,n} \exp(i\phi_n), \tag{7}$$

where $A_{X,n}$ and $A_{Y,n}$ are the amplitudes of the Fourier transform and ϕ_n the phase lag between the two bands. In order to reduce noise, the cross-spectrum is also computed for several light curve segments and averaged over segments and over frequency bins. The averaged cross-spectrum is denoted $\overline{C}_{XY,n}$. For an easier interpretation, the phase lag can be converted into a time lag,

$$\tau(\nu_j) = \phi(\nu_j)/(2\pi\nu_j), \tag{8}$$

from which we directly infer the time delay between the two time series. The error on the lag is dependent on the coherence. The coherence measures the level of linear correlation between two signals, which in our case corresponds to two light curves of different energy bands. The coherence is defined as

$$\gamma^2(\nu_j) = \frac{\left|\overline{C}_{XY}(\nu_j)\right|^2 - n^2}{\overline{P}_X(\nu_j)\overline{P}_Y(\nu_j)} \tag{9}$$

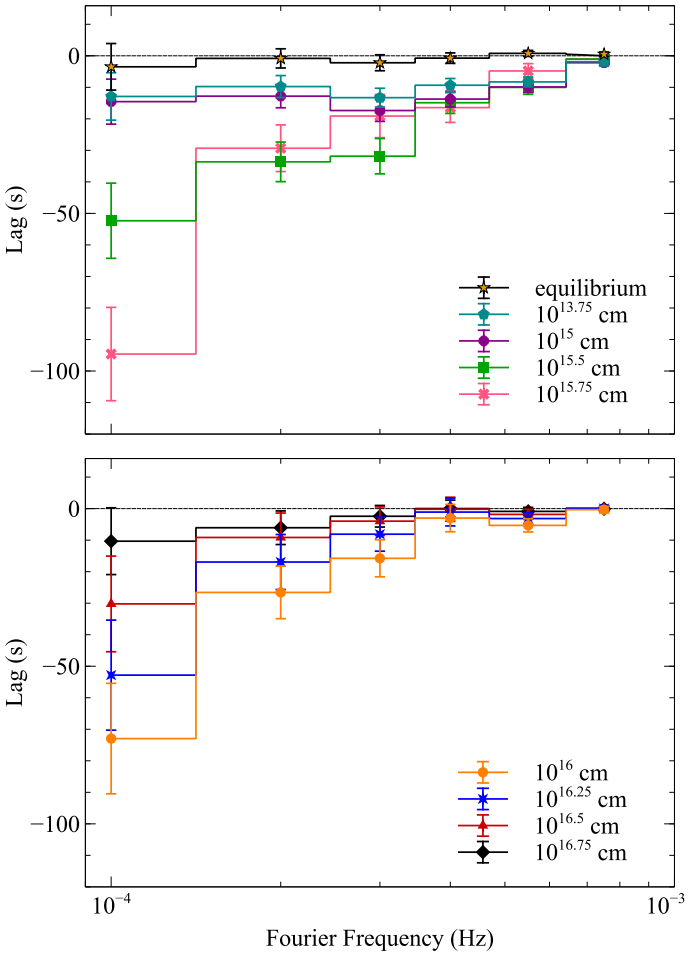

Fig. 6. Lag-frequency spectrum for a grid of distances of the warm absorber to the central source. A negative lag indicates that the soft band (0.3−1.0 keV) lags the hard (2.0−5.0 keV).

and takes values between 1 (for perfectly correlated signals) and 0 (for signals with no linear correlation). The n^2 is a bias term due to Poisson-noise contribution to the modulus square of the cross-spectrum (see for further details Uttley et al. 2014; Vaughan & Nowak 1997). The error on the phase lag is then defined as

$$\Delta\phi(\nu_j) = \sqrt{\frac{1 - \gamma^2(\nu_j)}{2\gamma^2(\nu_j) K M}} \tag{10}$$

where K and M respectively correspond to the number of frequencies and segments over which the periodogram and the cross-spectrum were averaged. Converted to the time domain, Eq. (10) takes the form

$$\Delta\tau = \Delta\phi/(2\pi\nu_j). \tag{11}$$

Through the application of these Fourier techniques, it is possible to detect the timing properties of the time series for a broad range of timescales. We applied these methods to the light curves we have generated from the simulated spectra, which account for the warm absorber response to changes in the ionizing continuum. Our results are presented below.

4.1. Lag-frequency spectrum

The lag-frequency spectrum is a common way to represent the time (or phase) lag between two time series as a function of

Fourier frequency. Mostly for AGN, this way of representing the timing properties of the light curves produces a very characteristic pattern consisting of two distinct signatures (e.g. Zoghbi et al. 2011; De Marco et al. 2013). At low frequencies, which correspond to long timescales, the hard photons from a given variation lag the soft photons from that same variation. This delay is thus called a hard lag, and can have a magnitude from tens to thousands of seconds. At higher frequencies, the sign of the lag is inverted. Therefore, on short timescales, the soft photons from a certain variation arrive after the hard photons from that same variation, which is called a soft lag. This behavior is often observed when selecting a soft (e.g., 0.3−1.0 keV) and hard (e.g., 2.0−5.0 keV) time series, and computing the cross-spectrum. Since the warm absorber greatly affects the soft X-rays, we investigate how the soft X-rays behave compared to the hard X-rays.

We use an EPIC-pn simulated time series in the soft band (0.3−1.0 keV) and compute its cross-spectrum with a harder band (2.0−5.0 keV). To compute the cross-spectrum we divided the data into contiguous segments of 10 ks each and a time bin of 500s, the same time resolution we have for the time-dependent concentrations. We do this for the same range of distances − of the warm absorber to the central source − that we used to compute the time-dependent concentrations. Our results are presented in Fig. 6. The upper panel shows the lag vs. frequency spectra for the equilibrium situation and for distances from $10^{13.75}$ up to $10^{15.75}$ cm. The lower panel shows the same but for distances from 10^{16} up to $10^{16.75}$ cm. For an equilibrium situation, represented by the stars in Fig. 4, the warm absorber responds instantaneously to changes in the ionizing continuum. Since the warm absorber has an instantaneous response to the source variability, we do not expect to observe a time delay between the more absorbed soft X-rays and the hard X-rays. This is the case for warm absorbers located at smaller distances from the black hole. As seen in Fig. 4, for radial distances up to 10^{14} cm, the warm absorber appears to be in equilibrium with the variability of the central source, responding instantaneously. For distances $\geq 10^{15.75}$ cm we observe in Fig. 4 that the warm absorber is no longer in equilibrium with the ionizing continuum. This non-equilibrium situation is characterized by a response time that causes a delay between the more absorbed photons and the continuum photons. This delay is detected in the lag-frequency spectrum we computed. The time lag between the soft and the hard photons is detected towards lower Fourier frequencies, indicating long timescales. The strongest delay appears to come from the region around $10^{15.75}$ cm. For even larger radial distances, the delay between the soft and the hard bands smooths away, which again agrees with what we expect, since for larger distances the warm absorber appears to be in a steady state, possibly in equilibrium with the average luminosity over time, and is not able to respond to the fast variability of the source. Hence, we proceed to analyze the most interesting situation for our work, which corresponds to the distance capable of producing the strongest time delay overall, $r = 10^{15.75}$ cm. As a reference, for component 1, $r \sim 10^{15.75}$ cm corresponds to a density $n \sim 1.1 \times 10^{7}$ cm^{-3}. The corresponding densities for the other components at these distances may be easily computed as $n_{\mathrm{comp}_Y} = \xi_{\mathrm{comp}_X} n_{\mathrm{comp}_X} / \xi_{\mathrm{comp}_Y}$, where X and Y can be any of the components in Table 1.

For the purpose of studying this situation in detail, we compute the cross-spectrum again, this time using narrow energy bins of interest. The energy bins are selected by taking into account the absorption features observed in the RGS spectrum of NGC 4051. An ideal feature to study the time behavior of the warm absorber is the Fe UTA complex (15−17 Å, see Fig. 4). This feature shows high opacity and it is very sensitive to flux variations (see e.g. Krongold et al. 2007). Furthermore, the Fe UTA complex is broader than a single absorption line, and so it also provides us with higher signal-to-noise ratio. Taking a time series from the simulated RGS light curves in this band, we compute its cross-spectrum with a broad EPIC-pn simulated light curve. For comparison, we also computed the cross-spectrum for another absorbed band, 12.5−14 Å, and for a band that shows only weak absorption, 26−27 Å. These results are shown in Fig. 7, together with the lag-frequency and coherence spectra for the hard and soft bands.

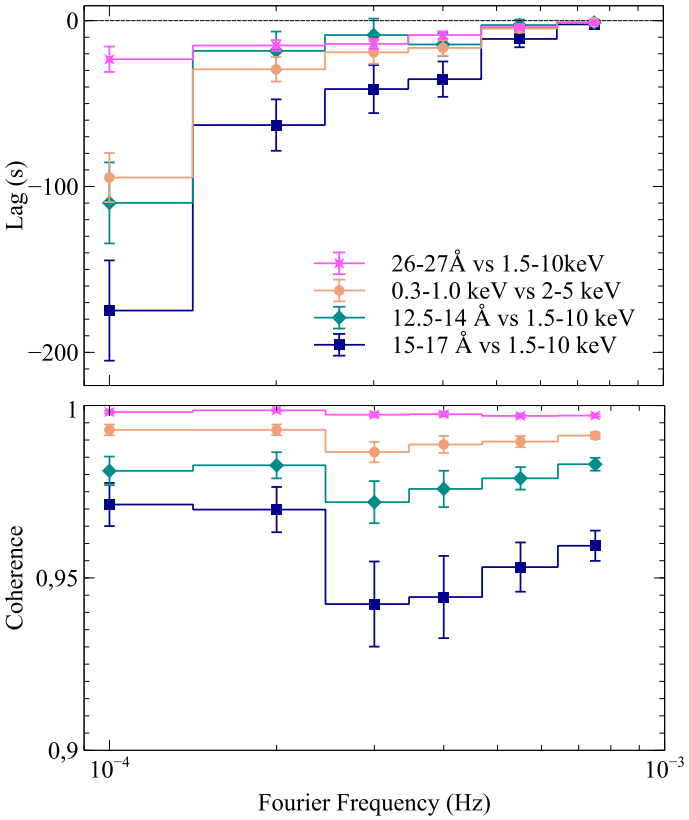

Fig. 7. Lag-frequency spectrum (*top*) and coherence spectrum (*bottom*) of several bands of interest for $r = 10^{15.75}$ cm. The labels are (from top to bottom) unabsorbed band RGS (26−27 Å) vs. broadband EPIC-pn (1.5−10 keV), soft band (0.3−1 keV) vs. hard band (2−5 keV) both from EPIC-pn, Ne blended absorption in the RGS band (12.5−14 Å) vs. broadband EPIC-pn (1.5−10 keV), and Fe UTA absorption feature in the RGS band (15−17 Å) vs. broadband EPIC-pn (1.5−10 keV). A negative lag indicates that the band of interest lags the reference band.

The time delay between the Fe UTA feature and the broad continuum band is ∼175 s, at a Fourier frequency of 10^{-4} Hz. In contrast, the time delay between the band that shows almost no absorption and the broadband continuum is only ∼25 s for the same frequency. Furthermore, the time delay between the absorbed 12.5−14 Å band and the continuum is ∼110 s. Even using EPIC-pn data, which are not as sensitive to the changes in these features, we observe a soft lag of ∼95 s at low frequencies. From these results alone we can conclude that a warm absorber with the characteristics of the one in NGC 4051, if located at a certain optimal distance from the central source ($10^{15.75}$ cm with our assumptions), would produce a time delay of ∼100 s between the more absorbed bands and the broad ionizing continuum on timescales of hours or longer. This lag, however, is

not to be interpreted directly as a response time. The lags are effectively diluted since only a small fraction of the total flux is being modulated by the variations of the absorbing features (for a discussion on lag dilution see e.g. Uttley et al. 2014).

As can been seen in the lower panel of Fig. 7, the coherence between the two energy bands also appears to show a small dependence on the absorption. For increasing lag, the coherence between the two bands is slightly reduced. However, the whole process still appears highly coherent, reaching a coherence of ~0.97 for the longest hard lag detected. Interestingly, the observed coherence at low frequencies for NGC 4051 is high, but not exactly 1. The observed coherence for NGC 4051 at low frequencies has a value of ~0.85 (Alston et al. 2013a). This could be due in part to the small effect of the warm absorber.

To further investigate the timing behavior, for several narrow energy bins covering the whole RGS spectral range we computed the lag-energy spectrum.

4.2. Lag-energy spectrum

The energy resolved lag spectrum, or lag-energy spectrum (Uttley et al. 2014), is an extremely valuable tool for our study, since we can relate it directly to the observed energy spectrum and assess the behavior of the lags at energies that are highly absorbed. Hence, we are able to directly link the lags to the regions in the spectrum where absorption plays a major role. Taking the cross-spectrum between each of the channels of interest vs. the reference band, it is possible to select a range of Fourier frequencies of interest and take the average, plotting then the average lag against energy. In this way we can build a lag-energy spectrum that contains the information of all the previously calculated lag-frequency spectra, but then taking into account a specific range of frequencies. This way of looking at time lags allows a comparison between the relative lag in several bands, providing a direct comparison of the behavior of the time lags and the energy spectrum, since both are a function of energy.

Taking into account the fact that any time delays between the more absorbed bands and the continuum appear to be negligible above $3{-}4 \times 10^{-4}$ Hz, we have considered the range of frequencies $1{-}3{\times}10^{-4}$ Hz to compute the lag-energy spectrum. In Fig. 8, we plot the transmission of the four warm absorber models, contained in our best fit to the averaged RGS spectrum, and the lag-energy spectrum for the computed grid of distances. As can be seen from Fig. 8, the regions in the energy spectra from where more direct continuum is removed by absorption from the outflowing gas, correspond to the regions of the lag-energy spectra where we see a stronger soft lag. The amplitude of the lags results from averaging in Fourier frequency and is therefore lower than the maximum lag observed in the lag-frequency spectrum. The lag appears to be greatest around distances of $10^{15.75}$ cm for the whole energy spectrum.

To assess the contribution of each warm absorber component to the lag-energy spectrum, we have redone the spectral simulations and cross-spectral products for each warm absorber component separately. This was once again done for the most interesting case, corresponding to a radial distance of $10^{15.75}$ cm, where a maximum lag is seen for the whole energy range. The results are shown in Fig. 9. When analyzing the lag-energy spectrum of each component separately, we see that the warm absorber that has a higher impact on the lags in this source is the one associated with the Fe UTA feature, since this is the most prominent feature in the whole energy spectrum, and it is also very sensitive to the flux variations (see Fig. 5). This corresponds to component 3, which has a mild ionization parameter

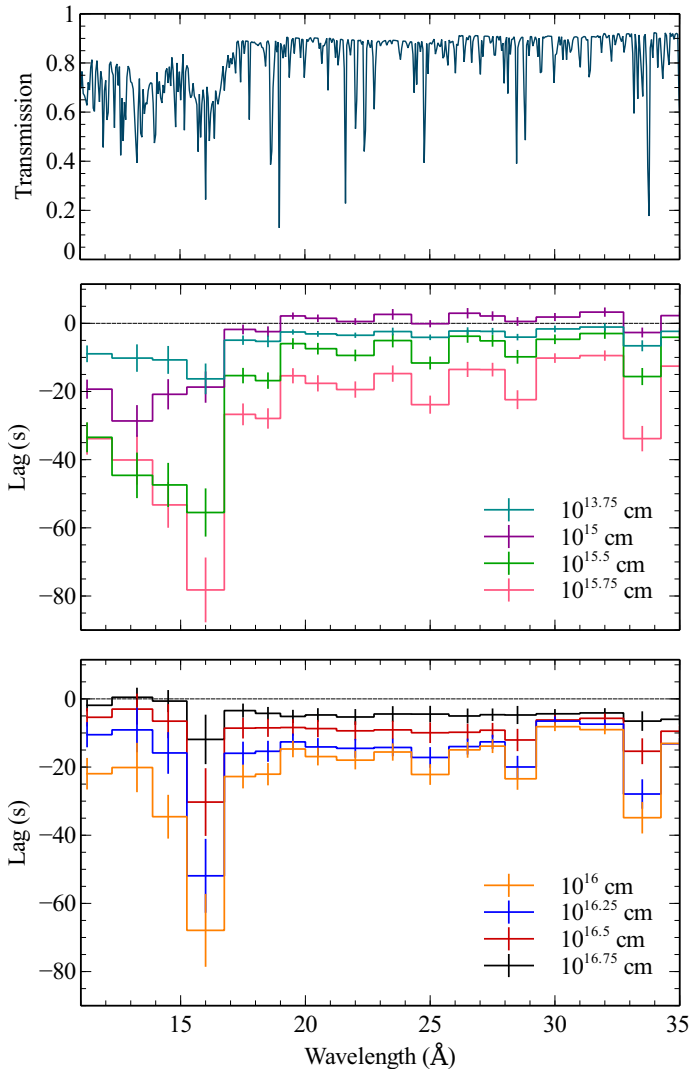

Fig. 8. Warm absorber transmission model (*top*) and lag-energy spectrum (*middle and bottom*) for the computed grid of distances. The reference band to compute the lag-energy spectrum is a broad EPIC-pn band (1.5−10 keV). We note that a negative lag indicates a soft lag, which means that the band of interest lags the broad reference band. This helps to easily match the lag-energy spectrum to the absorption features in the energy spectrum.

of $\log \xi \sim 2.6$. Component 1, has an ionization parameter close to the value of component 3, $\log \xi \sim 2.9$, and so it affects the same energy bands as component 3, contributing to a stronger effect at those energies. Component 2 is the component with the highest ionization parameter, $\log \xi \sim 3.7$, and so it is the major contributor at high energies (around 10−15 Å). Finally, the least ionized component, component 4, does not appear to have a major contribution. This can in part be explained by the low ionization of this component. At the same distance, component 4 will be much denser than the other components, and a higher density would result in a faster response time. However, since the column density of this component is much lower than the others, its contribution to absorption of the spectrum (see the transmission plot from Fig. 9), and therefore to the lags is minimal even at larger distances and/or lower densities.

We note that the response time is not only dependent on the density of gas, but it also depends on the ion species that play a stronger role for each component (see Eq. (1)). Therefore, the

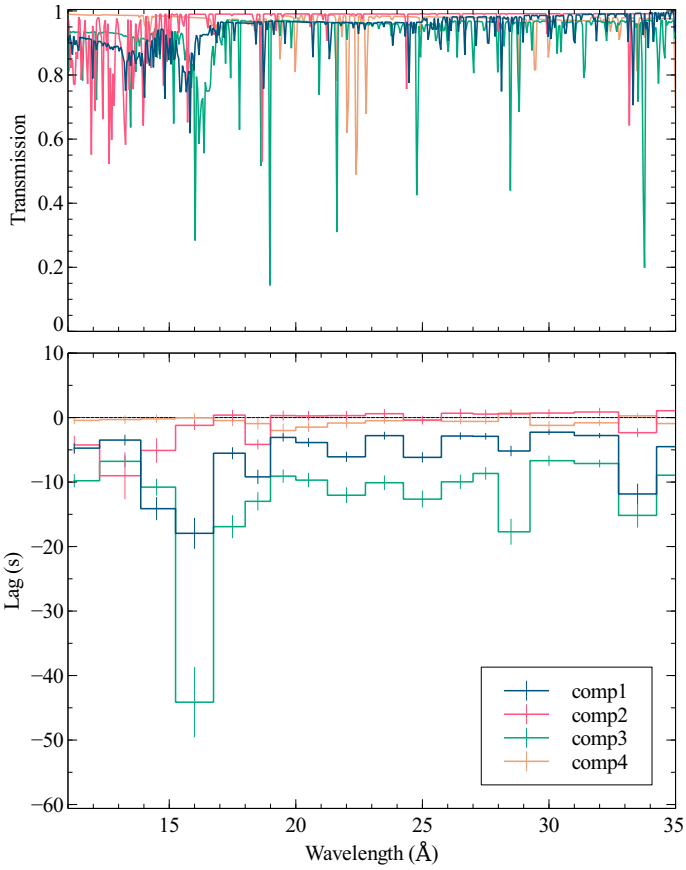

Fig. 9. Warm absorber transmission model and lag-energy spectrum for each warm absorber component separately for $r = 10^{15.75}$ cm. See Table 1 for the parameters of the gas components. We note that a negative lag indicates a soft lag, which means that the band of interest lags the broad reference band. This helps to easily match the lag-energy spectrum to the absorption features in the energy spectrum.

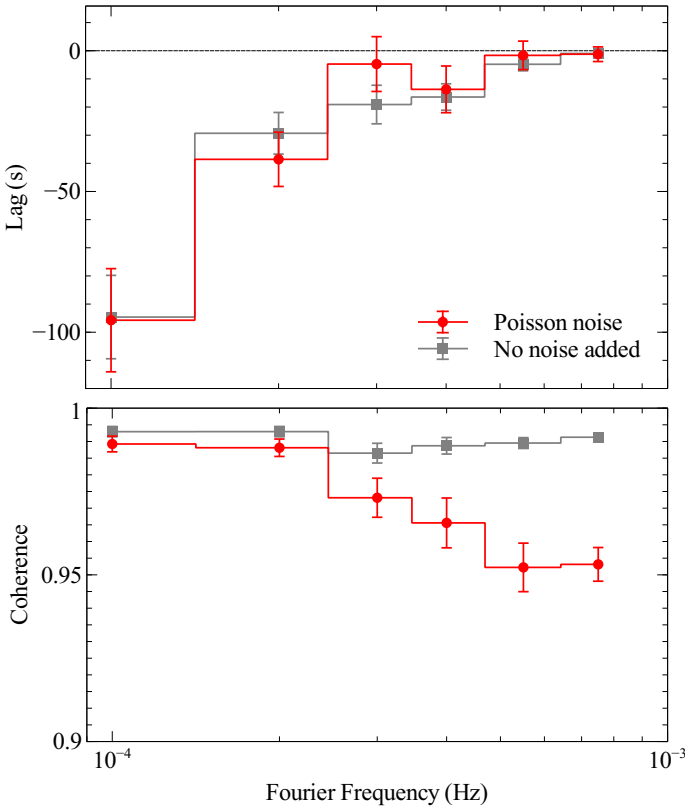

Fig. 10. Lag-frequency spectrum (*top panel*) and coherence spectrum (*lower panel*) between the soft (0.3−1.0 keV) and hard (2.0−5.0 keV) bands of the simulated light curves for EPIC-pn including Poisson noise.

contribution to the lags only scales linearly with density if the same warm absorber component is being considered.

5. Comparison to the real data

Having studied the pure effects that a variable warm absorber would introduce to the timing properties of the X-ray light curves of NGC 4051, we now compare our results with the observed data and discuss whether these effects could be detectable with currently available instruments and data.

5.1. Detectability

To assess the detectability level of these warm absorber effects we add Poisson noise when generating light curves from the simulated spectra. We perform this analysis for the soft (0.3−1.0 keV) and hard (2.0−5.0 keV) bands and compute the lag-frequency spectrum using the methods outlined in Sect. 4. The results are shown in Fig. 10.

As can be seen from the lag-frequency spectrum, Poisson noise does not play a major role at the Fourier frequencies of interest. It minimally increases the error bars on the computed lags and scatters the value of the lag slightly. This is to be expected since from the study of the power-spectrum of NGC 4051 it is possible to observe that the Poisson noise only has an effect at high Fourier frequencies (Alston et al. 2013a). Therefore, the effects on the lags are minimal. The coherence is also affected only towards higher Fourier frequencies. In this way, it is safe to say that the effects we discussed in the previous section are detectable using currently available data. This means that if the warm absorber in NGC 4051 was located at a radial distance of $\sim 10^{15.75}$ cm from the black hole, and if no other processes were at play, a soft lag would be expected at low frequencies.

5.2. Comparison to RGS data

We now compare the results we obtained from the simulated RGS data to the real observations. The lag-energy spectra that we presented in Figs. 8 and 9, were computed from simulated RGS data that include only the effects of the response of the warm absorber to the changes in flux of the ionizing continuum. The RGS spectra, owing to the higher spectral resolution of the RGS instrument, help us to distinguish which spectral features contribute more to the lags. We then computed the lag-energy spectrum using real RGS light curves, in bands of interest, to investigate whether it would be possible to detect a signature of the warm absorber in the real data even in the presence of external continuum processes, which we did not consider in the simulations. We find that for the real data, the size of the error bars makes it difficult to say whether the lag is associated with the warm absorber or if the continuum processes dominate. To examine this further we performed a simple test. We consider that the photons that reach the warm absorber have already been subjected to the continuum processes that produce the dominant observed hard lag at low Fourier frequencies, and thus already carry a time delay associated with these processes. When these

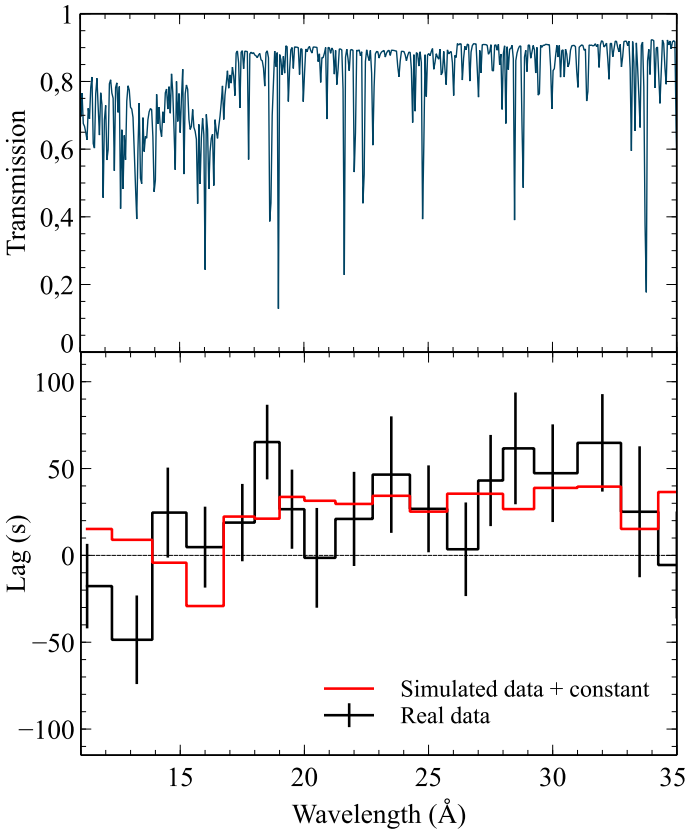

Fig. 11. Warm absorber transmission model (*top*) and lag-energy spectrum (*bottom*). The lag-energy spectrum from simulated data, at $r = 10^{15.75}$ cm (see Fig. 8) with an additive constant of 49.1 s, was fitted to the observed lag-energy spectrum, plotted in black, to obtain a χ^2 of 20.7 for 17 d.o.f. The simulated lag-energy spectrum with an offset, corresponding to the constant that resulted from the fit (∼50 s), is overplotted in red. The reference band to compute the lag-energy spectrum is a broad EPIC-pn band (1.5−10 keV). We note that a negative lag indicates a soft lag, which means that the band of interest lags the broad reference band. This helps to easily match the lag-energy spectrum to the absorption features in the energy spectrum.

photons reach the warm absorber and are subjected to the response time, this effect should be additive. Thus, the lag caused by the response time of the warm absorber should add to the previously carried lag. Hence, our simplified model consists in fitting the simulated lag-energy spectrum with an additive constant to the observed lag-energy spectrum. We find that adding a constant lag of ∼50 s provides the best fit from matching our simplified model to the data. These results are shown in Fig. 11. Therefore, we can conclude that it is not possible with this dataset to detect structure in the lag-energy spectrum that may indicate a signature of the response time of the warm absorber to changes in the ionizing continuum. Other datasets, and in particular future instrumentation with higher quality grating or calorimeter data may allow this test.

5.3. Effects on measured X-ray time lags

Understanding and disentangling the various components that play a role in the timing properties of the X-ray light curves of AGN is fundamental in order to break the degeneracies that spectral fitting alone perpetuates. It is then crucial to determine the level to which the effects of the variable warm absorber may affect the standard picture of the lag-frequency spectrum of AGN X-ray time series.

Compared to the previous work on the timing properties of NGC 4051 by Alston et al. (2013a), it is clear that a soft (negative) lag is not detected at low frequencies when using the whole 2009 dataset. We have performed the same analysis on the real data and our results agree with Alston et al. (2013a). The lag-frequency spectrum of NGC 4051, when considering the whole 2009 dataset, consists of a hard (positive) lag at low frequencies followed by a turnover that leads to a soft (negative) lag at higher frequencies. As mentioned earlier, the soft lag at high frequencies has been connected to a direct result of reflected emission of the hard coronal X-rays on the softer disk photons, causing a time delay between the direct hard X-ray emission and the reflected emission (Fabian et al. 2009). The variable warm absorber also causes a delay between soft and hard photons, however, only for long timescale variations (on the order of hours). Thus we do not expect the measured reverberation lags in this source to be affected by the variable warm absorber. However, the soft lag we detect at low frequencies (long timescales) due to the delayed response of the more absorbed energy bands compared to the ionizing continuum, can affect the measured hard lag at those frequencies. This could mean, in principle, that the intrinsic hard lag at low frequencies would have a higher amplitude if we were able to exclude the effect from the warm absorber.

Hard lags at low Fourier frequencies are common in AGN lag-frequency spectra, especially for systems with a relatively low mass such as NGC 4051 (De Marco et al. 2013). Therefore, we stress that understanding the effect of the warm absorber is necessary in order to fully grasp the nature of the hard lags in these sources.

5.4. Flux dependence

The shape of the SED and the variability amplitude of NGC 4051 are known to vary with flux level (Vaughan et al. 2001). To investigate the effects of these variations with flux level, Alston et al. (2013a) performed a flux resolved study of the lag-frequency spectrum of NGC 4051. Alston et al. (2013a) found that the lag-frequency spectrum of NGC 4051 is also variable. When considering only high flux segments, the lag-frequency spectrum resembles the one calculated with the whole time series. This behavior is expected since the high flux segments are also the most variable and will dominate the averaged cross-spectrum due to the higher Fourier amplitudes. On the other hand, the lag-frequency spectrum selecting only medium or low flux segments shows a transition at low Fourier frequencies (long timescales); a hard lag is no longer detected but a soft lag is observed instead. It has not yet been possible to physically explain this behavior. However, since the low flux lag-frequency spectrum resembles the soft lags produced by a warm absorber, we also performed this analysis on our simulated data.

Using the same reference mean flux levels as Alston et al. (2013a), we compute the flux resolved lag-frequency spectrum to find whether the soft lag we find due to the variable warm absorber could also be dependent on the flux level. We overplot in Fig. 12 the lag-frequency spectrum for the high, medium, and low flux level segments. We find that the soft lag we observe exclusively due to the variable warm absorber appears to be more significant when picking only low flux segments. The lag depends on delayed changes in the fraction of absorbed photons. When this fraction is large (e.g., at low fluxes) the lag is large, whereas when it is small (e.g., at high fluxes) the lag is small. From the simulated spectra, we have verified that these

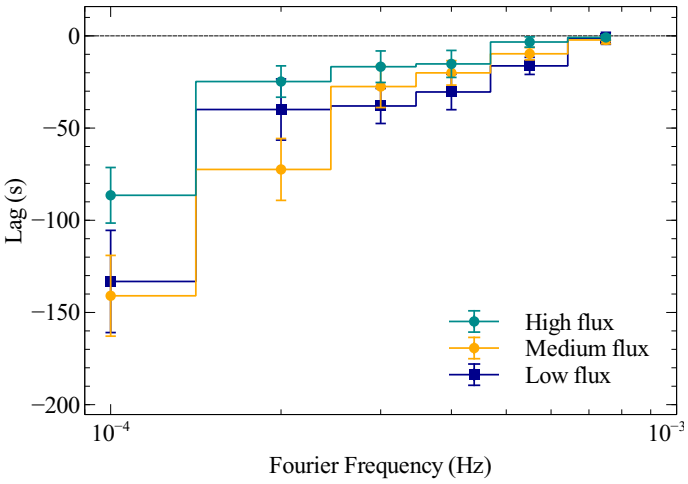

Fig. 12. Lag-frequency spectrum between the soft (0.3−1.0 keV) and hard (2.0−5.0 keV) bands of the simulated light curves for EPIC-pn, for different flux levels.

flux-dependent changes in the absorbed fraction of photons do occur for some absorption features, particularly for the Fe UTA feature, which is one of the main contributors to the lag. Additionally, different atomic transitions are affected by different ionization states, which result in different response times and responses at different timescales. We suggest that the flux dependence of the lags at low Fourier frequencies may be at least in part due to the ionization state of the gas, but investigating this complex behavior in detail goes beyond the scope of this paper and we will address it in future work. For the non-detection of a soft lag at low frequencies in the total/combined dataset, this could be due to the fact that the high flux states are dominated by other processes. The mechanism responsible for the hard lags at low frequencies might be enhanced at high flux levels and might dominate the other lag components.

5.5. Distance of the warm absorber

Previous studies of the complex spectrum of NGC 4051 have found the warm absorber to be located quite close to the black hole and ruled out a torus origin for the gas. Using a simple time-dependent photoionization model on ROSAT data, Nicastro et al. (1999) estimate the gas electron density to be $n \sim 10^8$ cm^{-3}, which yields a distance from the X-ray source of $\sim 7.4 \times 10^{15}$ cm. Krongold et al. (2007) were able to detect high- and low-ionization absorbers with *XMM-Newton* data, and derived a density of $n \sim 5.8{-}21 \times 10^6$ cm^{-3} and $n < 8.1 \times 10^7$ cm^{-3}, respectively, through time-resolved spectroscopy. These densities lead to an estimate for the distances of $1.3{-}2.6 \times 10^{16}$ cm for the high-ionization phase and of $<9 \times 10^{15}$ cm for the low-ionization phase. More recently with new *XMM-Newton* observations, Pounds & King (2013) identified a much more complex ionized outflow and propose that the wind is being shocked at a distance of 10^{17} cm, which places the warm absorber at distances of $<10^{17}$ cm. Our simulations indicate a maximum effect of the response time of the warm absorber on the X-ray time lags at distances of $\sim 0.3{-}1.0 \times 10^{16}$cm, which are comparable to the distance at which the broad-line region is located in this source (Denney et al. 2009). Furthermore, these distances correspond to gas densities in the range of $n \sim 0.4{-}3.0 \times 10^7$ cm^{-3} for the two major contributors to the lags, components 1 and 3. Therefore, if we take into account the existing estimates of the location (and density) of the warm absorber and compare them to our results, it appears that the low-frequency X-ray time lags in NGC 4051, measured by Alston et al. (2013a), are very possibly affected by the response of the gas to the source variability.

6. Conclusions

Working simultaneously with RGS and EPIC-pn data, we performed a detailed analysis using a time-dependent photoionization code in combination with spectral and Fourier spectral-timing techniques. We applied this method to the extensive *XMM-Newton* archival observations of the bright and highly variable Seyfert 1 galaxy NGC 4051, whose spectrum has revealed a complex multicomponent wind. As a result, we have shown that warm absorbers have the potential to introduce time lags between the most highly absorbed bands relative to the continuum for a certain range of gas densities and/or distances. The time delay is produced by the response of the gas to changes in the ionizing source, either by photoionization or radiative recombination.

We find that, in the absence of any other lag mechanisms, a soft (negative) lag, on the order of ∼100 s, is detected when computing the spectral-timing products between the more absorbed energy bands from simulated RGS spectra and a broad continuum band from simulated EPIC-pn spectra, on timescales of hours. Furthermore, we also find that the absorbing gas can likewise produce a time delay between the broader soft and hard bands, both belonging to simulations of EPIC-pn spectra. This happens because the soft band appears to be generally more absorbed, and so even without the higher spectral resolution provided by RGS we can see the soft band lagging behind the hard for long timescales. A direct consequence of our results is that understanding the contribution of the recombining gas to the X-ray lags is vital information for interpreting the continuum lags associated with propagation and reflection effects in the inner emitting regions. We have shown that the effects of the warm absorber in this source are negligible on short timescales where the reverberation lag is found. However, on long timescales (∼hours) the response time of the absorber causes the soft photons to lag the hard photons by up to hundreds of seconds. This will have implications for the modeling of the observed hard lags, which have been measured to be only ∼50 s in NGC 4051, since the effect of the warm absorber is to dilute them or even produce dominant soft lags at low frequencies.

The range of gas distances that, under our assumptions, yield a stronger effect of the warm absorber are comparable to the existing estimates for the location of the warm absorber in NGC 4051. In the light of this we note that it is likely that the warm absorber plays a role in the observed X-ray time lags in this source. If this is the case, such effects can also help explain the observed soft lags at low frequencies for the low flux segments of the 2009 dataset from NGC 4051.

The results we present in this paper are specific to a case study we performed on NGC 4051 and its warm absorber. Assessing the effects of the warm absorber to the lags through future studies in which we will explore the parameter space will then allow us to disentangle the contribution from continuum processes and warm absorber responses in the lag-frequency and lag-energy spectrum of AGN. As mentioned earlier, one of the problems in the study of these systems through time-resolved spectroscopy are the timescales involved (on the order of minutes to hours), which result in limited photon counts, per time and energy bin. Moreover, there are also other processes playing a role on these timescales, namely continuum processes that produce the hard lag. When doing time-resolved spectroscopy

the gas response lags are not easily distinguished from the continuum lags, which may cause spurious measurements of the response time. Evaluating the level of uncertainty on these estimates goes beyond the scope of this paper. We stress that using spectral-timing analysis together with a time-dependent photoionization model is an extremely powerful method, not only to access the contribution of the warm absorber to the X-ray time lags, but also having the potential to provide important diagnostics on the warm absorber location and gas density, which we will explore in future work. Furthermore, the method can be applied to other sources and warm absorber configurations allowing for a wide range of studies. Indeed, recent work by Kara et al. (2016) shows that some AGN with soft lags at low Fourier frequencies are also highly absorbed, highlighting a possible connection between variable absorption and low-frequency lags in other sources. These spectral-timing methods will allow the study of the warm absorber response on even shorter timescales and at higher spectral resolution than have ever been possible. With the current dataset on NGC 4051, it is not yet possible to determine whether the lag is associated with the warm absorber; however, a higher signal-to-noise grating or calorimeter data may enable this test. Looking farther ahead, ATHENA (Nandra et al. 2013) will allow these methods to be routinely used to study the detailed time response of individual absorption components, and will allow us to map AGN outflows in exquisite detail.

Acknowledgements. We would like to thank Jelle Kaastra for providing us with his code as a basis for the development of this method. We would also like to thank Martin Heemskerk for all his help and advice on numerically solving stiff differential equations. Furthermore, we would like to thank Gary Ferland, Gerard Kriss, Daniel Proga, and the participants of the Lorentz Center workshop "The X-ray Spectral-Timing Revolution" (February 2016) for useful discussions. We would also like to thank the anonymous referee for helpful comments. Simon Vaughan was the PI of the 2009 observation of NGC 4051. C. V. Silva acknowledges support from NOVA (Nederlandse Onderzoekschool voor Astronomie). The Space Research Organization of the Netherlands is supported financially by NWO, the Netherlands Organization for Scientific Research. In this work we made use of observations obtained with *XMM-Newton*, an ESA science mission with instruments and contributions directly funded by ESA Members States and the USA (NASA).

References

Alston, W. N., Vaughan, S., & Uttley, P. 2013a, MNRAS, 435, 1511
Alston, W. N., Vaughan, S., & Uttley, P. 2013b, MNRAS, 429, 75
Arav, N., Moe, M., Costantini, E., et al. 2008, ApJ, 681, 954
Arévalo, P., & Uttley, P. 2006, MNRAS, 367, 801
Behar, E., Rasmussen, A. P., Blustin, A. J., et al. 2003, ApJ, 598, 232
Crenshaw, D. M., & Kraemer, S. B. 2012, ApJ, 753, 75
Crenshaw, D. M., Kraemer, S. B., Boggess, A., et al. 1999, ApJ, 516, 750
Crenshaw, D. M., Kraemer, S. B., & George, I. M. 2003, ARA&A, 41, 117
De Marco, B., Ponti, G., Cappi, M., et al. 2013, MNRAS, 431, 2441
Denney, K. D., Watson, L. C., Peterson, B. M., et al. 2009, ApJ, 702, 1353
Di Matteo, T., Springel, V., & Hernquist, L. 2005, Nature, 433, 604
Fabian, A. C. 2012, ARA&A, 50, 455
Fabian, A. C., Zoghbi, A., Ross, R. R., et al. 2009, Nature, 459, 540
Ferland, G. J., Porter, R. L., van Hoof, P. A. M., et al. 2013, Rev. Mex. Astron. Astrofis., 49, 137
Hardcastle, M. J., Evans, D. A., & Croston, J. H. 2007, MNRAS, 376, 1849
Kaastra, J. S., Mewe, R., & Nieuwenhuijzen, H. 1996, in UV and X-ray Spectroscopy of Astrophysical and Laboratory Plasmas, eds. K. Yamashita, & T. Watanabe, 411
Kaastra, J. S., Raassen, A. J. J., Mewe, R., et al. 2004, A&A, 428, 57
Kaastra, J. S., Detmers, R. G., Mehdipour, M., et al. 2012, A&A, 539, A117
Kalberla, P. M. W., Burton, W. B., Hartmann, D., et al. 2005, A&A, 440, 775
Kara, E., Fabian, A. C., Cackett, E. M., et al. 2013, MNRAS, 434, 1129
Kara, E., Alston, W., & Fabian, A. 2016, Astron. Nachr., 337, 473
Kotov, O., Churazov, E., & Gilfanov, M. 2001, MNRAS, 327, 799
Kraemer, S. B., Crenshaw, D. M., Gabel, J. R., et al. 2006, ApJS, 167, 161
Krolik, J. H., & Kriss, G. A. 1995, ApJ, 447, 512
Krongold, Y., Nicastro, F., Elvis, M., et al. 2007, ApJ, 659, 1022
Lodders, K., Palme, H., & Gail, H.-P. 2009, Landolt Börnstein (Springer), 44
Mathews, W. G., & Ferland, G. J. 1987, ApJ, 323, 456
McHardy, I. M., Papadakis, I. E., Uttley, P., Page, M. J., & Mason, K. O. 2004, MNRAS, 348, 783
Nandra, K., Barret, D., Barcons, X., et al. 2013, ArXiv e-prints [arXiv:1306.2307]
Nicastro, F., Fiore, F., Perola, G. C., & Elvis, M. 1999, ApJ, 512, 184
Pounds, K. A., & King, A. R. 2013, MNRAS, 433, 1369
Pounds, K. A., & Vaughan, S. 2011, MNRAS, 413, 1251
Press, W. H., Teukolsky, S. A., Vetterling, W. T., & Flannery, B. P. 1992, Numerical recipes in FORTRAN, The art of scientific computing (CUP)
Reeves, J. N., Nandra, K., George, I. M., et al. 2004, ApJ, 602, 648
Steenbrugge, K. C., Fenovčík, M., Kaastra, J. S., Costantini, E., & Verbunt, F. 2009, A&A, 496, 107
Uttley, P., McHardy, I. M., Papadakis, I. E., Cagnoni, I., & Fruscione, A. 1999, Nucl. Phys. B Proc. Suppl., 69, 490
Uttley, P., Cackett, E. M., Fabian, A. C., Kara, E., & Wilkins, D. R. 2014, A&ARv, 22, 72
Vaughan, B. A., & Nowak, M. A. 1997, ApJ, 474, L43
Vaughan, S., Edelson, R., Warwick, R. S., Malkan, M. A., & Goad, M. R. 2001, MNRAS, 327, 673
Vaughan, S., Uttley, P., Pounds, K. A., Nandra, K., & Strohmayer, T. E. 2011, MNRAS, 413, 2489
Zoghbi, A., Uttley, P., & Fabian, A. C. 2011, MNRAS, 412, 59
Zoghbi, A., Fabian, A. C., Reynolds, C. S., & Cackett, E. M. 2012, MNRAS, 422, 129